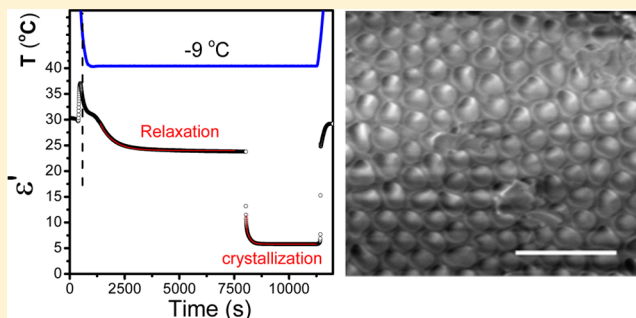


## Kinetics of Ice Nucleation Confined in Nanoporous Alumina

Yasuhito Suzuki,<sup>†</sup> Martin Steinhart,<sup>‡</sup> Hans-Jürgen Butt,<sup>†</sup> and George Floudas<sup>\*,§</sup><sup>†</sup>Max Planck Institute for Polymer Research, 55128 Mainz, Germany<sup>‡</sup>Institut für Chemie neuer Materialien, Universität Osnabrück, D-49069 Osnabrück, Germany<sup>§</sup>Department of Physics, University of Ioannina, 45110 Ioannina, Greece

**ABSTRACT:** The nucleation mechanism of water (heterogeneous/homogeneous) can be regulated by confinement within nanoporous alumina. The kinetics of ice nucleation is studied in confinement by employing dielectric permittivity as a probe. Both heterogeneous and homogeneous nucleation, obtained at low and high undercooling, respectively, are stochastic in nature. The temperature interval of metastability extends over  $\sim 4$  and  $0.4$  °C for heterogeneous and homogeneous nucleation, respectively. Nucleation within a pore is spread to all pores in the template. We have examined a possible coupling of all pores through a heat wave and a sound wave, with the latter being a more realistic scenario. In addition, dielectric spectroscopy indicates that prior to crystallization undercooled water molecules relax with an activation energy of  $\sim 50$  kJ/mol, and this process acts as precursor to ice nucleation.



undercooled water molecules relax with an activation energy of  $\sim 50$  kJ/mol, and this process acts as precursor to ice nucleation.

## I. INTRODUCTION

Efforts to study highly supercooled water are based on decreasing the available sample volume.<sup>1–14</sup> For example, water can be supercooled down to  $-38$  °C or even down to  $-70$  °C<sup>2</sup> by confinement, respectively, to micrometer or nanometer sizes. Under these conditions, it will crystallize via homogeneous nucleation. In most cases, however, water will freeze at higher temperatures by impurities via heterogeneous nucleation. In a recent study,<sup>15</sup> we demonstrated that the nucleation mechanism of water can be regulated by confinement within self-ordered nanoporous aluminum oxide (AAO). AAOs contain arrays of cylindrical nanopores with pore diameters ranging from 25 to 400 nm that are uniform in length and diameter. They can be considered as a model system<sup>16</sup> in investigating confinement effects not only on water crystallization but also on polymer crystallization<sup>17–20</sup> and liquid crystal phase manipulation.<sup>21,22</sup> Within AAOs there is a change of freezing mechanism from heterogeneous nucleation to homogeneous nucleation with decreasing pore diameter from 400 to 25 nm. In addition, we proposed<sup>15</sup> a correlation between the ice nucleation mechanism and the type of crystal structure: heterogeneous nucleation in larger pores gives the well-known hexagonal ice ( $I_h$ ), whereas homogeneous nucleation in smaller pores results in a predominant cubic ice ( $I_c$ ) instead. These results lead to a phase diagram of water under confinement. It contains a (stable) predominant  $I_c$  form in pores having diameters below about 35 nm. The proposed phase diagram for confined water can have possible technical application in various research areas where water exists in confined spaces including construction materials like cement. The differential scanning calorimetry (DSC) curves of hardened Portland cement pastes,<sup>23</sup> for example, contain two

well-defined peaks at  $-41$  and  $-23$  °C. According to the proposed phase diagram, these peaks may reflect the homogeneous/heterogeneous freezing of water in different pore structures. In addition, the suppression of heterogeneous nucleation and dominance of homogeneous nucleation in the smaller AAO pores suggests the absence of heterogeneous nucleation sites (that is, impurities) from the pores because of the small pore volume. Based on this finding, we suggest that the majority of impurities in water have sizes that exceed 35 nm. This observation opens up the possibility of employing AAO templates as filters for ultrapure water.

This study combines structural and dynamic probes to provide fundamental insight into the kinetics of ice nucleation in the confined space of AAO. For this purpose, we employ dielectric permittivity as a fingerprint of ice nucleation under confinement in conjunction with structural probes (X-rays). We explore the heterogeneous and homogeneous nucleation kinetics for water located inside 400 and 25 nm, respectively, by performing temperature quench experiments to different final crystallization temperatures. Although both processes are stochastic in nature, the temperature interval within which metastability is different for heterogeneous and homogeneous nucleation. Furthermore, before the onset of crystallization, water molecules undergo a structural relaxation. This relaxation is suggested to be associated with the formation of additional hydrogen bonds.

Received: July 1, 2015

Revised: August 4, 2015

Published: August 4, 2015

## II. EXPERIMENTAL SECTION

**i. Water Infiltration.** Water infiltrates AAOs fast as evidenced from dielectric spectroscopy, scanning electron microscopy, and wide-angle X-ray scattering. Capillary imbibition at the microscale is described by the Lucas–Washburn relation (LW):<sup>24</sup>

$$h(t) = \sqrt{\frac{\gamma R \cos \theta}{2\eta} t} \quad (1)$$

where  $h$  is the imbibition length (the pore length in this case),  $\gamma$  is the surface tension,  $\theta$  is the equilibrium contact angle,  $R$  is the pore radius, and  $\eta$  is the viscosity. Employing  $h = 100 \mu\text{m}$ ,  $R = 100 \text{ nm}$ ,  $\eta(20^\circ\text{C}) = 0.001 \text{ Pa}\cdot\text{s}$ , and  $\gamma = 0.071 \text{ N/m}$  results in millisecond filling times that broadly agrees with our experience of fast infiltration. Even the pressure built up due to the fact that the pores are closed to the end will not prolong filling to significant time scales.<sup>25</sup> We mention here that modifications of the LW relation have been proposed that account for the dynamic contact angle effect;<sup>26</sup> however, testing the LW equation is beyond the scope of the present investigation.

**ii. Scanning Electron Microscopy (SEM) and Cryo-SEM.** Empty AAO was imaged with a LEO Gemini 1530 scanning electron microscope. Operation acceleration voltages were from 0.75 to 6 kV. Water was infiltrated into the AAO membranes and immediately frozen with liquid nitrogen. Subsequently, the AAO was mechanically broken inside the cryo-preparation chamber under a vacuum of  $2 \times 10^{-5}$  mbar at  $-180^\circ\text{C}$  to expose cross sections. Then image was taken with a Nova600 NanoLab – Dualbeam scanning electron microscope/focused ion beam (FIB) system equipped with a cryogenic preparation chamber (Quorum Technologies) under cryoscopic conditions at an acceleration voltage of 2 kV. The detector used was a “through the lens” secondary electron detector.

**iii. Dielectric Spectroscopy (DS).** Dielectric measurements were performed at temperatures in the range of  $-90$  to  $30^\circ\text{C}$ , at atmospheric pressure, under isochronal conditions ( $f = 1 \text{ MHz}$ ) using a Novocontrol Alpha frequency analyzer (frequency range from  $10^{-2}$  to  $10^6 \text{ Hz}$ ) as a function of temperature. For the water infiltrated self-ordered AAO samples, a 10 mm electrode was placed on top of the templates whereas the Al in the bottom of the templates served as the second electrode. The measured dielectric spectra were corrected for the geometry by using two capacitors in parallel (composed of  $\epsilon^*_{\text{W}}$  and  $\epsilon^*_{\text{A}}$ , being the complex dielectric function of water and alumina, respectively, and the measured total impedance was related to the individual values through  $1/Z^* = 1/Z^*_{\text{W}} + 1/Z^*_{\text{A}}$ ). In all cases, the complex dielectric permittivity  $\epsilon^* = \epsilon' - i\epsilon''$ , where  $\epsilon'$  is the real and  $\epsilon''$  is the imaginary part, was obtained at 1 MHz. This allows calculating the real and imaginary parts of the dielectric permittivity as a function of the respective volume fractions by using  $\epsilon^*_{\text{M}} = \epsilon^*_{\text{W}}\phi_{\text{W}} + \epsilon^*_{\text{A}}\phi_{\text{A}}$ .

**iv. Wide-Angle X-ray Scattering (WAXS).** The  $\Theta/2\Theta$  scans were taken with a D8 Advance X-ray diffractometer (Bruker). The X-ray tube (KRISTALLOFLEX 780) generator with a Cu anode was operating at a voltage of 40 kV and a current of 30 mA. An aperture (divergence) slit of 0.3 mm, a scattered-radiation (antiscatter) variable slit (V12) together with a monochromator slit of 0.1 mm and a detector slit of 1 mm were employed. A scintillation counter with a 95% quantum yield for the Cu radiation was employed as the

detector. Scans in the  $2\Theta$ -range from  $20$  to  $50^\circ$  (Figure 1d) and  $22$  to  $28^\circ$  (Figure 6b) in steps of  $0.02^\circ$  were made. The AAO

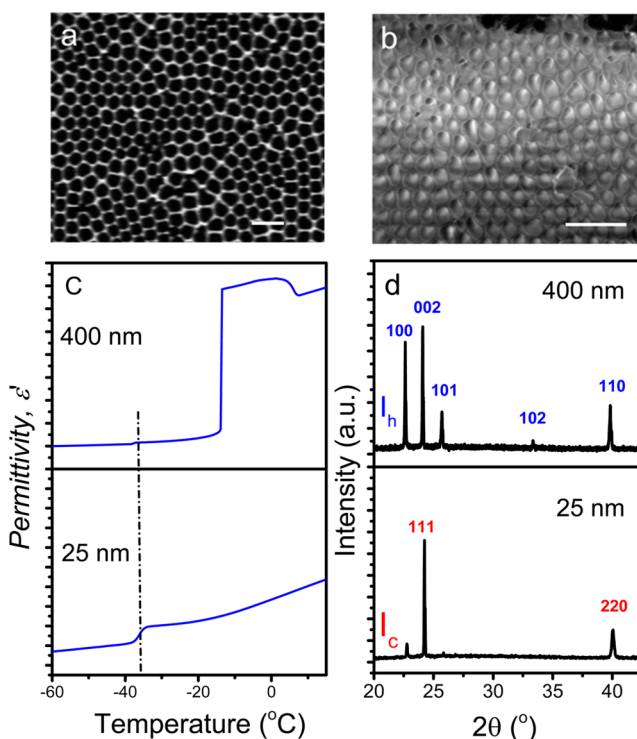


**Figure 1.** SEM images of (a) empty AAO pores of 400 nm pore diameter and (b) water frozen within the same pores at  $-100^\circ\text{C}$ . The white scale bars correspond to (a) 1 and (b) 2  $\mu\text{m}$ . (c) Temperature dependence of the as measured dielectric permittivity for water inside AAO with pore diameter of 400 nm (top) and 25 nm (bottom) measured at a frequency of 1 MHz. The vertical line indicates the homogeneous nucleation temperature. (d) Diffraction patterns of water frozen at  $-50^\circ\text{C}$  within AAO with pore diameters of 400 nm (top) and 25 nm (bottom). The main reflections corresponding to hexagonal ice ( $I_h$ ) and to cubic ice ( $I_c$ ) are shown in blue and red, respectively.

pore axes were oriented parallel and the AAO surface was oriented perpendicularly to the plane of the incident and scattered X-ray beams.

## III. RESULTS AND DISCUSSION

Figure 1 summarizes the “static” properties of ice nucleation confined within AAO templates.<sup>15</sup> It depicts SEM images of empty AAO with 400 nm pore diameter (Figure 1a) and of water infiltrated into the same AAO membranes (Figure 1b). Subsequently, the high dielectric permittivity of water and its temperature-dependence was employed as a fingerprint of ice nucleation. It is well-known that the temperature dependent dielectric permittivity,  $\epsilon'_s(T)$ , is a sensitive probe of phase transformations.<sup>21,27</sup> Figure 1c compares the dielectric permittivity curves of water inside AAO with pore diameters of 400 and 25 nm under isochronal conditions. The dielectric permittivity of water inside AAO with a pore diameter of 400 nm gradually decreases upon cooling. This decrease is due to some water evaporation, except in the range from  $7.5$  to  $1.2^\circ\text{C}$ . The steep increase in the vicinity of the density anomaly is attributed to changes of the effective dipole moment due to dipole–dipole interactions. According to the Kirkwood–Fröhlich theory, the static dielectric permittivity of polar liquids

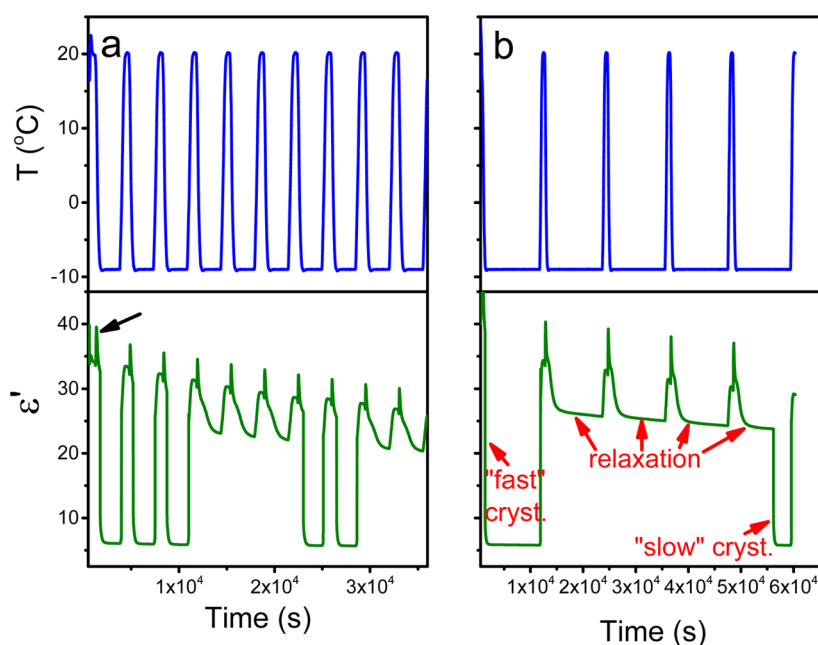


**Figure 2.** Temperature profiles (top) and dielectric permittivity curves (as measured) (bottom) for water inside AAO with a pore diameter of 400 nm. All measurements refer to water crystallization at  $-9\text{ }^{\circ}\text{C}$  measured at a frequency of 1 MHz. Isochronal measurements refer to  $-9\text{ }^{\circ}\text{C}$  for different time intervals: 40 min (a) or for 3 h (b). The black arrow in (a) indicates the density anomaly of water. Different processes are indicated in (b): “fast” crystallization, “slow” crystallization and relaxation.

with short-range interactions between molecules,  $\epsilon'_s$ , can be expressed as<sup>28,29</sup>

$$\Delta\epsilon = \epsilon'_s - \epsilon_{\infty} = \frac{1}{3\epsilon_0} Fg \frac{\mu^2}{k_B T} \frac{N_0}{V} \quad (2)$$

Here,  $F = \epsilon'_s(\epsilon_{\infty} + 2)^2 / [3(2\epsilon'_s + \epsilon_{\infty})]$  is the local field,  $N_0/V$  is the number density of dipoles expressed as  $(\rho/M)N_A$ , where  $\rho$  is the mass density and  $M$  is the molar mass, and  $\mu$  is the dipole moment.  $g$  is the Kirkwood–Fröhlich dipole orientation correlation function,  $g = \mu^2/\mu_{\text{gas}}^2$ , defined as the ratio of the mean-squared dipole moment measured in a dense system divided by the same quantity obtained in a noninteracting case. Thus, changes in  $g$  can account for the peculiar  $\epsilon'_s(T)$  dependence in the vicinity of the density anomaly of water. Upon further cooling, water inside AAO with a pore diameter of 400 nm froze at  $-13.6\text{ }^{\circ}\text{C}$  to a permittivity of  $\sim 4$ . Based on these findings we concluded that the majority of 400 nm pores contain *impurities* that initiate crystallization by heterogeneous nucleation. Crystallization in the smaller pores was fundamentally different. Only a single step in dielectric permittivity was observed in the range from  $-36$  to  $-38\text{ }^{\circ}\text{C}$ . Therefore, in AAO with a pore diameter of 25 nm (Figure 1c), water crystallized exclusively by homogeneous nucleation at low temperatures.

Confinement within AAO not only alters the ice nucleation mechanism but also affects the crystal structure.<sup>15,30–38</sup> Figure 1d shows diffraction patterns of ice within AAO with pore diameters of 400 and 25 nm taken at  $-50\text{ }^{\circ}\text{C}$ . The diffraction patterns are distinctly different. In the case of ice within 400 nm pores they correspond to the common hexagonal ice ( $I_h$ ). However, in the smaller pore, the dominant peaks correspond to the (111) and (220) reflections of cubic ice ( $I_c$ ), revealing a predominantly cubic ice. This form is stable under annealing and persists up to the melting point.<sup>15</sup>

We further explored the kinetics of heterogeneous and homogeneous ice nucleation at low and high supercooling,

respectively. The method of choice was again DS, taking advantage of the sensitivity of the dielectric permittivity to ice formation (Figure 1c). Figure 2 gives the dielectric permittivity traces during consecutive cooling/heating runs for water located inside AAO with a pore diameter of 400 nm. Results are shown for the crystallization kinetics from an initial temperature of  $20\text{ }^{\circ}\text{C}$  to the same final temperature of  $-9\text{ }^{\circ}\text{C}$  and for different waiting times at the final temperature. The temperature profile during these runs is also shown for comparison. Three features in the permittivity traces deserve special attention. First,  $\epsilon'(T)$  displays a peak during cooling (arrow in Figure 2a) at a temperature corresponding to the density anomaly of water. Second, the traces clearly demonstrate that heterogeneous ice nucleation is a probabilistic effect.<sup>39,40</sup> Under some circumstances, ice nucleates immediately after reaching the final temperature (called “fast” crystallization in Figure 2b); otherwise, it can take much longer times (that is, “slow” crystallization; see, for example, the last crystallization event in Figure 2b). Third, when water crystallizes, it does so in all pores at once, leading, surprisingly, to the same limiting permittivity value ( $\epsilon'_{\infty} \sim 5\text{--}6$ ). By studying different crystallization temperatures, we conclude that these findings agree with the notion that heterogeneous ice nucleation is a stochastic process. As such, it depends on the pore size, the degree of supercooling, and the time interval.

The third observation on the identical  $\epsilon'_{\infty}$  values upon crystallization deserves more attention. It suggests that pores somehow “communicate”, that is, the news on the crystallization in one pore is spread not only to the neighboring pores but to all pores in the template. The obvious communication through some liquid layer at the top of the template is excluded since this would enforce a heterogeneous nucleation independent from the pore size contrary to the experimental findings. Here we consider two possibilities: a heat wave and a sound (pressure) wave.

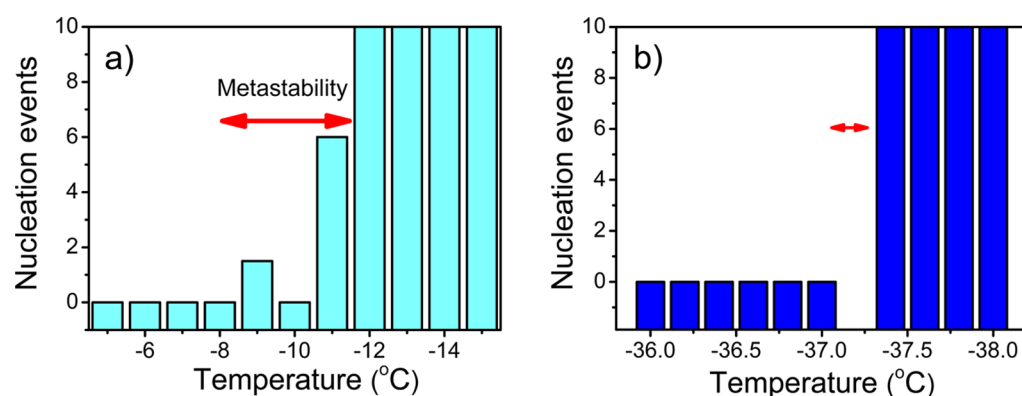


**Figure 3.** Number of nucleation events as a function of crystallization temperature following temperature jumps from 20 °C to different final temperatures for water inside AAO with pore diameter of 400 nm (a) and 25 nm (b). Red arrows indicate the range of metastability. Notice the much smaller temperature range in (b) corresponding to homogeneous nucleation.

We first discuss the heat wave produced by freezing water within a single pore. We assume an array of parallel cylindrical pores with radius  $r$  ( $=200$  nm) and length  $l$  ( $=100$   $\mu\text{m}$ ). With a density of ice of  $917$   $\text{kg}/\text{m}^3$ , the mass of ice within a single pore is  $m_i = 1.15 \times 10^{-14}$  kg. Employing the latent heat,  $L = 333$  kJ/kg, the heat released by ice formation in a single pore is  $Q_i = 3.8 \times 10^{-9}$  J. Such a heat will raise the temperature by  $\Delta T = 157$  K ( $\Delta T = Q_i/c_i m_i$ , where  $c_i$  is the heat capacity of ice  $= 2.093$  kJ/kg  $\text{K}^{-1}$ ). With such a temperature gradient, ice would melt instantly. However, the heat is dissipated fast. The time scale of temperature equilibration corresponds to 3 ns in the radial direction ( $t = r^2/4\kappa$ , where  $\kappa = 1.2 \times 10^{-5}$   $\text{m}^2/\text{s}$  is the thermal diffusivity of alumina) and 0.4 ms along the whole AAO thickness,  $l$  ( $t = l^2/2\kappa$ ). In addition, phonon scattering in low dimensional systems with large surface-to-volume ratios (like AAOs) can lead to a drastic reduction in thermal conductivity.<sup>42,43</sup> In any case, a heat wave is unlikely to couple all pores.

An alternative hypothesis is that sound (pressure waves) couples the pores. A sound wave with velocity  $u = (C_{11}/\rho)^{1/2}$  (with an elastic constant for alumina of  $C_{11} \sim 500$  GPa and a density  $\rho \sim 3.8$   $\text{g}/\text{cm}^3$ )<sup>43</sup> of  $\sim 1.1 \times 10^4$  m/s takes a fraction of a *picosecond* to traverse a distance of 400 nm. As to the origin of a sound wave, upon water crystallization, the modulus increases by many orders of magnitude (practically from zero to about 10 GPa<sup>45</sup>). This together with the expansion of ice in the pores upon freezing exerts a stress on the pore walls (the shear modulus of alumina is  $\sim 170$  GPa<sup>44</sup>) and to a friction across the interface. Above a certain stress, energy is released in the form of sound waves in pretty much the way that seismic waves are traveling during an earthquake.<sup>45</sup> A sound wave with a velocity of  $1.1 \times 10^4$  m/s can travel across the whole template in less than a microsecond and communicate the “news” to the remaining pores. This effect, observed for both heterogeneous and homogeneous nucleation, deserves a separate study as a function of pore size and pore fraction (porosity).

The number of nucleation events within AAO with pore diameters of 400 and 25 nm at different final temperatures corresponding to heterogeneous and homogeneous nucleation, respectively, are depicted in Figure 3. The term “nucleation event” refers to the sharp decrease in  $\epsilon'$  due to ice nucleation; a value of 0 (10) means that in a series of ten successive experiments no (always) nucleation took place; a value of 2 means that in a series of ten successive experiments ice nucleation took place only twice. The results for the

heterogeneous ice nucleation in 400 nm pores reveal that metastability is observed for final temperatures within the range from  $-8$  to  $-11$  °C. At temperatures above  $-8$  °C, water was unable to crystallize, whereas at temperatures below about  $-12$  °C ice was always formed. The range of metastability extends over  $\sim 4$  °C for heterogeneous ice nucleation under conditions of low undercooling. The same procedure was repeated for ice nucleation within 25 nm pores by following the  $\epsilon'(T)$  traces to lower temperatures (Figure 3b). It shows a much smaller range of metastability of at most  $\sim 0.4$  °C. The small range of metastability for homogeneous nucleation is consistent with some of the reported homogeneous ice nucleation rates.<sup>5</sup> Assuming a single nucleation event per pore and a pore volume of  $v \sim 5 \times 10^{-14}$   $\text{cm}^3$  (for 25 nm pores), a nucleation rate of  $J \sim 10^{14}$   $\text{cm}^{-3}\text{s}^{-1}$  at 235 K gives a freezing rate of  $Jv \sim 5$   $\text{s}^{-1}$ . On the other hand, nucleation rates close to some reported values<sup>2,3</sup> of  $\sim 10^{10}$   $\text{cm}^{-3}\text{s}^{-1}$  would give too low freezing rates to be observed experimentally. This point can be further explored, for example, by performing nucleation rate measurements by fast calorimetry with the same AAO templates.

The DS traces contain information on the relaxation of undercooled water as well as on the time scales involved in ice formation. This is depicted, for example, in Figure 4 where the evolution of dielectric permittivity is shown for a final crystallization temperature of  $-9$  °C. This is well within the metastability window for heterogeneous ice nucleation in 400 nm-AAO (Figure 3a). The curve depicted in Figure 4 corresponds to the “slow” crystallization event of Figure 2b. As mentioned with respect to Figure 2b, crystallization is occurring either within 200 s after reaching the final temperature (that is, “fast” crystallization, triggered by temperature variations occurring during temperature stabilization) or much later (that is, “slow” crystallization) as shown in Figure 4. After reaching the final temperature, the permittivity relaxes from a value of about 31 to a value of 25 with a characteristic time that is extracted by fitting with an exponential function. The characteristic *relaxation* times have a temperature dependence that will be discussed subsequently with respect to Figure 5. At longer times, slow *crystallization* sets in.

The characteristic “relaxation” and “crystallization” times for the heterogeneous nucleation kinetic experiments for water within 400 nm AAO are shown in Figure 5. The figure shows characteristic times for final temperatures in the range from  $-5$  to  $-13$  °C. Invariably, *fast* crystallization occurs within 200 s after reaching the final temperature (blue region in Figure 5). A

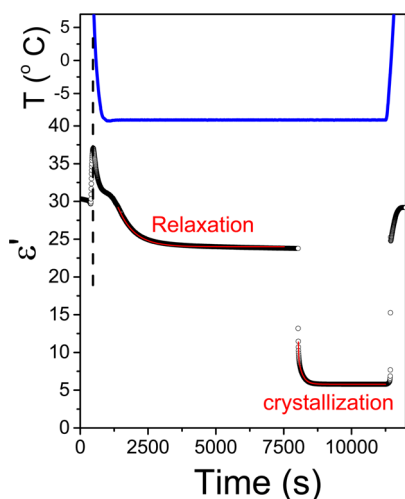


**Figure 4.** Temperature profile (top) and evolution of dielectric permittivity (bottom) for water inside AAO with 400 nm pore diameter. The vertical dashed line gives the maximum value of permittivity that corresponds to the density anomaly of water. Red lines give the result of a fit to the relaxation process using a single exponential and to the crystallization process using a sum of two exponentials. The characteristic times corresponding to the “relaxation” and “crystallization” events are reported in Figure 5.

careful examination of the temperature profile during this process revealed that it occurs within the temperature variations ( $\pm 0.2$  K) occurring during temperature stabilization. However, heterogeneous nucleation is a stochastic process, and when nucleation is not triggered by these temperature fluctuations, then ice nucleation can take much longer (see, for example, the solid triangle in Figure 5a corresponding to the “slow” crystallization event in Figure 4 or 2b). In the absence of “fast” crystallization and before the onset of “slow” crystallization, a *relaxation* of undercooled water takes place. From these results, the temperature dependence of the relaxation times can be extracted, and the result is plotted in Figure 5b. The characteristic relaxation times within the narrow temperature interval of metastability show an Arrhenius temperature dependence

$$\tau = \tau_0 \exp\left(\frac{E}{RT}\right) \quad (3)$$

with  $\tau_0 = 5.6 \times 10^{-12}$  s being the time in the limit of very high temperatures, and an activation energy,  $E$ , of  $\sim 50$  kJ/mol. Such activation energy corresponds to the formation of few hydrogen bonds and suggests some reorganization (that is, relaxation) of the undercooled water molecules in confinement. As we will discuss below with the help of X-rays, this reorganization does not lead to crystallization but may act as precursors to nucleation.

The kinetics of homogeneous ice nucleation was studied next by employing both dynamics/kinetic and structural probes. The dielectric permittivity ( $f = 1$  MHz) is followed for water inside AAO with pore diameter of 25 nm by making consecutive cooling/heating runs but to different final temperatures (Figure 6a). The final temperatures were  $-10$ ,  $-20$ ,  $-30$ , and  $-40$  °C.

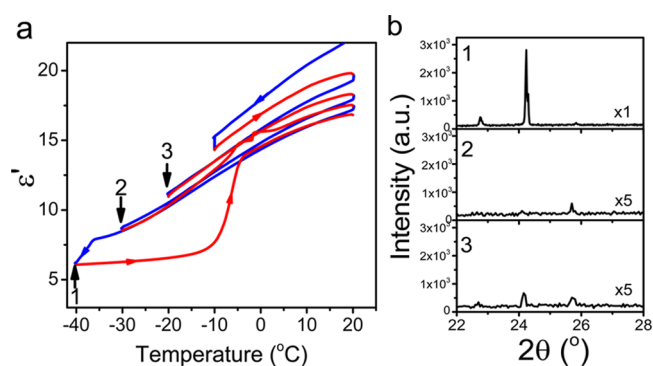


**Figure 6.** (a) Dielectric permittivity during consecutive cooling (blue curves)/heating (red curves) of water inside AAO with a pore diameter of 25 nm. The template was cooled from 20 °C to different final temperatures ( $-10$ ,  $-20$ ,  $-30$ , and  $-40$  °C) where stayed for 2 h. (b) Diffraction patterns obtained ex situ for (top) a template that was cooled to  $-50$  °C (cooling speed of 5 °C/min), (middle) the same template cooled at  $-30$  °C (cooling speed of 5 °C/min), and (bottom) cooled to  $-20$  °C (cooling speed of 5 °C/min). The diffraction patterns taken at  $-30$  and  $-20$  °C are multiplied by a factor of 5. Arrows give the corresponding annealing temperatures in (a).

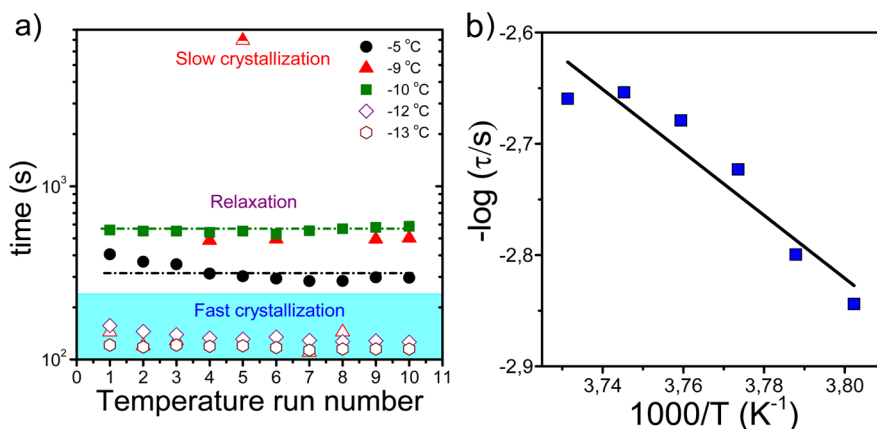


**Figure 5.** (a) Characteristic time corresponding to fast (empty symbols) and slow time constant of crystallization (half-filled symbol) and relaxation before crystallization (filled symbols) obtained for water inside AAO templates with a pore diameter of 400 nm plotted as a function of run number (from Figure 2). The characteristic times from different final crystallization temperatures are shown. Lines are guides for the eye at two “relaxation” experiments. (b) Mean relaxation time plotted as a function of inverse temperature. The line is the result of a linear fit.

At these temperatures, the sample stayed for 2 h and the dielectric permittivity was continuously monitored. Subsequently, the structural aspects were studied by *ex situ* WAXS at the same temperatures, and the results are depicted in Figure 6b. For the cooling/heating run to a limiting temperature of  $-10\text{ }^{\circ}\text{C}$ , it can be observed that the  $\epsilon'(T)$  curve is not completely reversible due to some unavoidable evaporation at  $-10\text{ }^{\circ}\text{C}$ . The subsequent cooling/heating run to a limiting temperature of  $-20\text{ }^{\circ}\text{C}$  (point 3 in Figure 6a) is nearly completely reversible (due to the lower evaporation at this temperature). The structure at this temperature corresponds to amorphous supercooled water as indicated by the absence of any sharp diffraction peaks (the shallow peaks are due to some water condensation). The next cooling/heating run to a limiting temperature of  $-30\text{ }^{\circ}\text{C}$  does not initiate any crystallization as expected by the results shown in Figure 3 and confirmed by WAXS. However, cooling to below  $-38\text{ }^{\circ}\text{C}$  results to ice nucleation and to a nonreversible dielectric permittivity curve. On heating, the  $\epsilon'(T)$  values remain constant up to the melting point at  $\sim -5\text{ }^{\circ}\text{C}$ . Moreover, the ice structure formed under these conditions corresponds to a predominantly cubic ice as discussed earlier (Figure 6b).

#### IV. CONCLUSIONS

The combined analyses using dielectric spectroscopy and X-ray scattering techniques could capture the details of the kinetics of ice nucleation under confinement. We found that both heterogeneous and homogeneous nucleation, obtained at low and high undercooling, respectively, are stochastic in nature, involving variable degrees of metastability. The temperature interval of metastability extends over  $\sim 4$  and  $0.4\text{ }^{\circ}\text{C}$  for heterogeneous and homogeneous nucleation, respectively. Nucleation within a single pore is spread to all pores in the template. Two possible mechanisms of coupling between pores through a heat wave and a sound wave are discussed with the latter being a more realistic scenario. Finally, prior to crystallization, undercooled water molecules relax with an activation energy of  $\sim 50\text{ kJ/mol}$ , corresponding to the formation of few hydrogen bonds. This process is seen as a precursor to ice nucleation.

#### AUTHOR INFORMATION

##### Corresponding Author

\*E-mail: gfloudas@uoi.gr (G.F.).

##### Notes

The authors declare no competing financial interest.

#### ACKNOWLEDGMENTS

The current work was supported by the operational program of the NSRF "Aristeia" cofinanced by the European Union and the Greek state. Sample preparation by C. Hess and H. Tobergte as well as SEM investigations by M. Kappl and M. Müller are gratefully acknowledged.

#### REFERENCES

- Huang, J.; Bartell, L. S. Kinetics of Homogeneous Nucleation In the Freezing of Large Water Clusters. *J. Phys. Chem.* **1995**, *99*, 3924–3931.
- Manka, A.; Pathak, H.; Tanimura, S.; Wölk, S.; Strey, R.; Wyslouzil, B. E. Freezing Water in No-Man's Land. *Phys. Chem. Chem. Phys.* **2012**, *14*, 4505–4516.
- Stan, C. A.; Schneider, G. F.; Shevkoplyas, S. S.; Hashimoto, M.; Ibanescu, M.; Wiley, B. J.; Whitesides, G. M. A Microfluidic Apparatus

for the Study of Ice Nucleation In Supercooled Water Drops. *Lab Chip* **2009**, *9*, 2293–2305.

(4) Duft, D.; Leisner, T. Laboratory Evidence for Volume-Dominated Nucleation of Ice In Supercooled Water Microdroplets. *Atmos. Chem. Phys.* **2004**, *4*, 1997–2000.

(5) Hagen, D. E.; Anderson, R. J.; Kassner, J. Homogeneous Condensation-Freezing Nucleation Rate Measurements for Small Water Droplets In an Expansion Cloud Chamber. *J. Atmos. Sci.* **1981**, *38*, 1236–1243.

(6) Angell, C. A. Supercooled Water. *Annu. Rev. Phys. Chem.* **1983**, *34*, 593–630.

(7) Limmer, D. T.; Chandler, D. Phase Diagram of Supercooled Water Confined to Hydrophilic Nanopores. *J. Chem. Phys.* **2012**, *137*, 044509.

(8) Steytler, D. C.; Dore, J. C.; Wright, C. J. Neutron Diffraction Study of Cubic Ice Nucleation In a Porous Silica Network. *J. Phys. Chem.* **1983**, *87*, 2458–2459.

(9) Morishige, K.; Kawano, K. Freezing and Melting of Water In a Single Cylindrical Pore: The Pore-Size Dependence of Freezing and Melting Behavior. *J. Chem. Phys.* **1999**, *110*, 4867–4872.

(10) Dore, J. Structural Studies of Water in Confined Geometry by Neutron Diffraction. *Chem. Phys.* **2000**, *258*, 327–347.

(11) Findenegg, G. H.; Jähnert, S.; Akcakayiran, D.; Schreiber, A. Freezing and Melting of Water Confined in Silica Nanopores. *ChemPhysChem* **2008**, *9*, 2651–2659.

(12) Johari, G. P. Origin of the Enthalpy Features of Water in 1.8 nm Pores of MCM-41 and the Large  $C_p$  Increase at 210 K. *J. Chem. Phys.* **2009**, *130*, 124518.

(13) Tombari, E.; Johari, G. P. On the State of Water in 2.4 nm Cylindrical Pores of MCM from Dynamic and Normal Specific Heat Measurements. *J. Chem. Phys.* **2013**, *139*, 064507.

(14) Li, K.; Xu, S.; Shi, W.; He, M.; Li, H.; Li, S.; Zhou, X.; Wang, J.; Song, Y. Investigating the Effects of Solid Surface on Ice Nucleation. *Langmuir* **2012**, *28*, 10749–10754.

(15) Suzuki, Y.; Duran, H.; Steinhart, M.; Kappl, M.; Butt, H.-J.; Floudas, G. Homogeneous Nucleation of Predominantly Cubic Ice Confined In Nanoporous Alumina. *Nano Lett.* **2015**, *15*, 1987–1992.

(16) Masuda, H.; Fukuda, K. Ordered Metal Nanohole Arrays Made by a Two-Step Replication of Honeycomb Structures of Anodic Alumina. *Science* **1995**, *268*, 1466–1468.

(17) Duran, H.; Steinhart, M.; Butt, H.-J.; Floudas, G. From Heterogeneous to Homogeneous Nucleation of Isotactic Poly(propylene) Confined to Nanoporous Alumina. *Nano Lett.* **2011**, *11*, 1671–1675.

(18) Suzuki, Y.; Duran, H.; Steinhart, M.; Butt, H.-J.; Floudas, G. Homogeneous Crystallization and Local Dynamics of Poly(ethylene oxide) (PEO) Confined to Nanoporous Alumina. *Soft Matter* **2013**, *9*, 2621–2628.

(19) Suzuki, Y.; Duran, H.; Akram, W.; Steinhart, M.; Floudas, G.; Butt, H.-J. Multiple Nucleation Events and Local Dynamics of Poly( $\epsilon$ -caprolactone) (PCL) Confined to Nanoporous Alumina. *Soft Matter* **2013**, *9*, 9189–9198.

(20) Suzuki, Y.; Duran, H.; Steinhart, M.; Butt, H.-J.; Floudas, G. Suppression of Poly(ethylene oxide) Crystallization In Diblock Copolymers of Poly(ethylene oxide)-*b*-Poly( $\epsilon$ -caprolactone) Confined to Nanoporous Alumina. *Macromolecules* **2014**, *47*, 1793–1800.

(21) Grigoriadis, C.; Duran, H.; Steinhart, M.; Kappl, M.; Butt, H.-J.; Floudas, G. Suppression of Phase Transitions in a Confined Rod-like Liquid Crystal. *ACS Nano* **2011**, *5*, 9208–9215.

(22) Duran, H.; Hartmann-Azanza, B.; Steinhart, M.; Gehrig, D.; Laquai, F.; Feng, X.; Mullen, K.; Butt, H.S.; Floudas, G. Arrays of Aligned Supramolecular Wires by Macroscopic Orientation of Columnar Mesophases. *ACS Nano* **2012**, *6*, 9359–9365.

(23) Bager, D. H.; Sellevold, E. J. Ice Formation in Hardened Cement Paste, Part I- Room Temperature Cured Pastes With Variable Moisture Contents. *Cem. Concr. Res.* **1986**, *16*, 709–720.

(24) Washburn, E. W. The Dynamics of Capillary Flow. *Phys. Rev.* **1921**, *17*, 273–283.

- (25) Stroberg, W.; Keten, S.; Liu, W. K. Hydrodynamics of Capillary Imbibition Under Nanoconfinement. *Langmuir* **2012**, *28*, 14488–14495.
- (26) Phan, V. N.; Nguyen, N. T.; Yang, C.; Joseph, P.; Djeghlaf, L.; Bourrier, D.; Gue, A. M. Capillary Filling in Closed End Nanochannels. *Langmuir* **2010**, *26*, 13251–13255.
- (27) Stangenberg, R.; Grigoriadis, C.; Butt, H.-J.; Müllen, K.; Floudas, G. Switchable Dielectric Permittivity With Temperature and Dc-bias In a Semifluorinated Azobenzene Derivative. *Colloid Polym. Sci.* **2014**, *292*, 1939–1948.
- (28) Kremer, F.; Schoenhals, A. *Broadband Dielectric Spectroscopy*; Springer: Berlin, 2002.
- (29) Floudas, G. In *Polymer Science: A Comprehensive Reference*; Matyjaszewski, K., Möller, M., Eds.; Elsevier BV: Amsterdam, 2012; Vol. 2.32.
- (30) Malkin, T. L.; Murray, B. J.; Brukhno, A. V.; Anwar, J.; Salzmann, C. G. Structure of Ice Crystallized From Supercooled Water. *Proc. Natl. Acad. Sci. U. S. A.* **2012**, *109*, 1041–1045.
- (31) Mayer, E.; Hallbrucker, A. Cubic Ice From Liquid Water. *Nature* **1987**, *325*, 601–602.
- (32) Murray, B. J.; Knopf, D. A.; Bertram, A. K. The Formation of Cubic Ice under Conditions Relevant to Earth's Atmosphere. *Nature* **2005**, *434*, 202–205.
- (33) Shilling, J. E.; Tolbert, M. A.; Toon, O. B.; Jensen, E. J.; Murray, B. J.; Bertram, A. K. Measurements of Vapor Pressure of Cubic Ice and Their Implication for Atmospheric Ice Clouds. *Geophys. Res. Lett.* **2006**, *33*, L17801.
- (34) Arnold, G. P.; Finch, E. D.; Rabideau, S. W.; Wenzel, R. G. Neutron-diffraction Study of Ice Polymorphism III. Ice Ic. *J. Chem. Phys.* **1968**, *49*, 4365–4369.
- (35) Hansen, T. C.; Koza, M. M.; Kuhs, W. F. Formation and Annealing of Cubic Ice: I. Modeling of Stacking Faults. *J. Phys.: Condens. Matter* **2008**, *20*, 285104.
- (36) Malkin, T. L.; Murray, B. J.; Salzmann, C. G.; Molinero, V.; Pickering, S. J.; Whale, T. F. Stacking Disorder In Ice I. *Phys. Chem. Chem. Phys.* **2015**, *17*, 60–76.
- (37) Russo, J.; Romano, F.; Tanaka, H. New Metastable Form of Ice and its Role In the Homogeneous Crystallization of Water. *Nat. Mater.* **2014**, *13*, 733–739.
- (38) Johari, G. P. Water's Size-dependent Freezing to Cubic Ice. *J. Chem. Phys.* **2005**, *122*, 194504.
- (39) Cross, M. C.; Hohenberg, P. C. *Rev. Mod. Phys.* **1993**, *65*, 851–1112.
- (40) Goh, L.; Chen, K.; Bhamidi, V.; He, G.; Kee, N. C. S.; Kenis, P. J. A.; Zukoski, C. F.; Braatz, R. D. A Stochastic Model for Nucleation Kinetics Determination in Droplet-based Microfluidic Systems. *Cryst. Growth Des.* **2010**, *10*, 2515–2521.
- (41) Sugisaki, M.; Suga, H.; Seki, S. Calorimetric Study of the Glassy State. IV. Heat Capacities of Glassy Water and Cubic Ice. *Bull. Chem. Soc. Jpn.* **1968**, *41*, 2591–2599.
- (42) Maldovan, M. Sound and Heat Revolutions in Phononics. *Nature* **2013**, *503*, 209–217.
- (43) Neogi, S.; et al. Tuning Thermal Transport in Ultrathin Silicon Membranes by Surface Nanoscale Engineering. *ACS Nano* **2015**, *9*, 3820–3828.
- (44) Munro, R. G. Evaluated Material Properties for Sintered alumina. *J. Am. Ceram. Soc.* **1997**, *80*, 1919–1928.
- (45) Godio, A.; Rege, R. B. The Mechanical Properties of Snow and Ice of an Alpine Glacier Inferred by Integrating Seismic and GPR Methods. *J. Appl. Geophysics* **2015**, *115*, 92–99.